scientific reports

OPEN

Analysis of entropy production in a bi-convective magnetized and radiative hybrid nanofluid flow using temperature-sensitive base fluid (water) properties

Tapas Barman [1], S. Roy [1✉] & Ali J. Chamkha [2]

The heat transport characteristics, flow features, and entropy-production of bi-convection buoyancy induced, radiation-assisted hydro-magnetic hybrid nanofluid flow with thermal sink/source effects are inspected in this study. The physical characteristics of hybrid nanofluids (water-hosted) are inherited from the base liquid (water) and none has considered the physical characteristics of base liquid (water) in the study of temperature-sensorial hybrid nanofluid investigations, though the water physical characteristics are not constants in temperature variations. So, the temperature-sensorial attributes of base liquid (water) are taken into account for this hybrid nanofluid ($Cu + Al_2O_3 +$ water) flow analysis. The mathematical forms of the flow configuration (i.e., the set of coupled, nonlinear PDE form of governing equations) are solved by utilizing the subsequent tasks: (i) congenial transformation; (ii) quasilinearization; (iii) methods of finite differences to form block matrix system, and (iv) Varga's iterative algorithm. The preciseness of the whole numerical procedure is ensured by restricting the computation to follow strict convergence conditions. Finally, the numerically extracted results representing the impacts of various salient parameters on different profiles (F, G, H), gradients, and entropy production are exhibited in physical figures for better perception. A few noticeable results are highlighted as: velocity graph shows contrast behaviour under assisting and opposing buoyancy; temperature ($G(\xi, \eta)$) is dropping for heightening heat source (Q) surface friction remarkably declines with the outlying magnetic field (St); thermal transport confronts drastic abatement under radiation (R_1), and St; the characteristics Reynolds and Brinkman numbers promote entropy. Furthermore, the bounding surface acts as a strong source of S_G-production. Summarizations are listed at the end to quantify percentage variations.

List of symbols

B_0	Outlying magnetic field
C_p	Specific heat capacitance
g	Gravity
k	Conductivity (thermal)
L	Reference length
q_r	Radiation heat flux
Q_0	Heat sink/source
β	Coefficient of volumetric expansion (thermal)
ϵ	Velocity ratio
ρ	Density
σ	Conductivity (electrical)
ϕ	Nanoparticle volume percentage
ψ	Streamfunction

[1]Mathematics Department, IIT Madras, Chennai 600036, India. [2]Faculty of Engineering, Kuwait College of Science and Technology, 35004 Doha District, Kuwait. ✉email: sjroy@iitm.ac.in

Abbreviations
EG   Entropy generation
BL   Boundary layer
HTI   Heat transfer irreversibility
FFI   Fluid friction irreversibility

Nondimentional functions
f, F   Streamfunction and velocity, respectively
G   Temperature

Subscripts
e   Condition at BL edge
w, ∞ Conditions at surface and outside of the BL edge, respectively
hnf Hybrid nanofluid
f   Fluid
s   Solid particles (nano)
sf   Nano-sized particles' shape factor
s_1, s_2 Cu And Al_2O_3 nanoparticles

The study of boundary layer (BL) flow along an inclined surface is enriched with real-life engineering applications like material processing, making glass fibres, solar energy systems, etc. Not only for its' wide application, but this particular geometric flow has also been a challenge to interested researchers to enumerate the flow phenomenon and heat-mass transport characteristics. In early studies, pioneer researchers[1–3] studied this geometry with different aspects of non-constant wall temperature, different inclination angle, different Prandtl numbers, etc. An experimental study of naturally convective flow for an inclined plate is presented by Al-Arabi and others[4]. Lewandowski[5] studied naturally convective flow along an inclined plate with a new approach. Jayaraj[6] inspected the thermophoretic effects on the flow for inclined plates. Later, a naturally convective flow was investigated for particulate suspension for inclined (isothermal) and vertical permeable plates by Ramadan and Chamkha[7,8]. A study of radiative MHD flow with variable porosity along an inclined plate was carried out by Chamkha and others[9]. Alam et al.[10] reported the MHD effect in combination with variable suction, radiation effect on a permeable flow over inclined plate (semi-infinite). The study of boundary layer (BL) flow for vertical and inclined surfaces is further continued by several researchers[11–16] considering different fluids (nanofluids, micro-polar fluids, etc.), and salient influencing factors like radiation, thermal injection/suction, outlying magnetic field, etc. An outlying magnetic field situating near an electrically conducting BL flow has numerous industrial engineering applications[17–22]. For example, in material processing, MHD effect may be used to get desired material structure[23]. Furthermore, the above-mentioned impactful factors in hybrid nanofluid flow encountered numerous applications in solar power technology, industrial areas, nuclear engineering, etc.,[24,25]. Recent studies[26,27] showed that hybrid nanofluid is the most sensitive one in thermal transport means than ordinary fluid and nanofluids. Many studies on radiation, thermal source/sink, and MHD effects on hybrid nanofluid flow are available in current literature and a few of them are referred in the following texts[28–33]. Moreover, in any thermo-dynamical system, the engineering efficiency of the system degrades due to irreversible heat loss. The enumeration of irreversibility i.e., entropy generation (EG) of a system may help to minimize the irreversible heat loss. The application and importance of the EG-study of radiative MHD hybrid nanofluid flow affected by thermal sink/sources from biomedical point of view is explored by P.B.A. Reddy[34]. Researchers[35] have found significant contributions of EG analysis in the studies of brain dynamics. Few more remarkable studies on this context are added as references[36–40].

It is a common practice to use water as a base liquid but water and water-hosted nanofluids are temperature-sensitive. Besides the thermos physical nanofluid characteristics are inherited from the hosted liquid, those properties are enhanced, advanced and empowered by the properties (thermos-physical) of emerging nanoparticles. But in recent studies, it is observed that base fluid properties have been ignored in temperature-sensitive nanofluid flow investigations. So, authors have investigated the temperature-sensorial characteristics (thermos-physical) of hybrid nanofluids in the light of temperature-sensorial water characteristics. That is, this study is taking account the temperature-sensorial properties of water into the model[41] for thermal relations utilizing empirical data[42] and used them to analyze the hybrid nano-liquid flow. Furthermore, the equations presenting the physical meaning of the considered physical system in mathematical form are solved using the following complicated numerical tasks[43,44]: (i) congenial transformation; (ii) quasilinearization; (iii) methods of finite-differences to form block matrix system, and (iv) Varga's iterative algorithm. The preciseness of the numerical approach is preserved by employing a strict convergence criterion.

Governing equations
From Table 1, μ_f and $(Pr)_f$ can be approximated at different temperatures as[41,42,44]

$$\mu_f(T) = \frac{1}{a_1 + a_2 T},\tag{1}$$

T (C)	ρ (g cm^{-3})	C_p (J 10^7 kg^{-1}K^{-1})	k (erg 10^5 cm^{-1}s^{-1}K^{-1})	μ (g 10^{-2}cm^{-1}s^{-1})	Pr
0	1.00228	4.2176	0.5610	1.7930	13.4
10	0.99970	4.1921	0.5800	1.3070	9.45
20	0.99821	4.1818	0.5984	1.0060	7.03
30	0.99565	4.1784	0.6154	0.7977	5.12
40	0.99222	4.1785	0.6305	0.6532	4.32
50	0.98803	4.1806	0.6435	0.5470	3.55

Table 1. Water properties vs. temperatures[44,45].

$$(Pr)_f(T) = \frac{1}{b_1 + b_2 T}, \tag{2}$$

where constant coefficients obtained from the curve fitting of thermos-physical data of water at various temperatures are b_1, b_2, c_1 and c_2 defined as:

$$\begin{pmatrix} b_1 \\ b_2 \\ c_1 \\ c_2 \end{pmatrix} = \begin{pmatrix} 53.41 \\ 2.43 \\ 0.068 \\ 0.004 \end{pmatrix}.$$

The hybrid nanofluid-base liquid correlations for various physical characteristics are given below[46]

$$\mu_{hnf}(T, \phi) = \frac{\mu_f(T)}{\sqrt{(1 - \phi)^5}}; \phi = \phi_{s_1} + \phi_{s_2}, \tag{3}$$

$$\frac{\rho_{hnf}(T, \phi)}{\rho_f(T)} = (1 - \phi) + \frac{\rho_{s_1}}{\rho_f(T)}\phi_{s_1} + \frac{\rho_{s_2}}{\rho_f(T)}\phi_{s_2}, \tag{4}$$

$$\frac{(\rho\beta)_{hnf}(T, \phi)}{(\rho\beta)_f(T)} = (1 - \phi) + \frac{(\rho\beta)_{s_1}}{(\rho\beta)_f(T)}\phi_{s_1} + \frac{(\rho\beta)_{s_2}}{(\rho\beta)_f(T)}\phi_{s_2}, \tag{5}$$

$$\frac{(C_p\rho)_{hnf}(T, \phi)}{(C_p\rho)_f(T)} = (1 - \phi) + \frac{(C_p\rho)_{s_1}}{(C_p\rho)_f(T)}\phi_{s_1} + \frac{(C_p\rho)_{s_2}}{(C_p\rho)_f(T)}\phi_{s_2}, \tag{6}$$

$$\frac{\sigma_{hnf}(T, \phi)}{\sigma_f(T)} = 1 + \frac{3\phi(\Psi_1 - \phi\sigma_f)}{\Psi_2 - (\Psi_1 - \phi\sigma_f)\phi}; \Psi_1 = (\sigma\phi)_{s_1} + (\sigma\phi)_{s_2}; \Psi_2 = \Psi_1 + 2\phi\sigma_f, \tag{7}$$

$$\frac{k_{hnf}(T, \phi)}{k_f(T)} = \frac{(sf - 1)k_f(T) + \frac{\Psi_3}{\phi} - (sf - 1)(\phi k_f(T) - \Psi_3)}{(sf - 1)k_f(T) + \phi k_f(T) + \left(\frac{\Psi_3}{\phi} - \Psi_3\right)}; \Psi_3 = (\phi k)_{s_1} + (\phi k)_{s_2}. \tag{8}$$

Here $sf\left(= \frac{3}{\Omega}\right)$ stands for nanoparticles' shape factor (Ω is the sphericity) (see Table 2) and the other terms $\phi, \mu_{hnf}, \rho_{hnf}, \beta_{hnf}, (C_p)_{hnf}, k_{hnf}, \sigma_{hnf}, \mu_f, \rho_f, \beta_f, (C_p)_f, k_f, \sigma_f, \phi_{s_1}, \rho_{s_1}, \beta_{s_1}, (C_p)_{s_1}, k_{s_1}, \sigma_{s_1}, \phi_{s_2}, \rho_{s_2}, \beta_{s_1}, (C_p)_{s_2}, k_{s_2}, \sigma_{s_2}$ are all given in the Nomenclature.

Table 2 shows that the variation in $\rho_f, (C_p)_f$ with respect to temperature is less than 1%. Combining this fact with the correlations (Eqs. 4–5) can be easily prove that the variation in $\rho_{hnf}, (C_p)_{hnf}$ is also less than 1%. So, from practical point of view, these two physical quantities can be considered as constant (see Table 3).

Consider a 2-D bi-convective (incompressible and steady) water-based hybrid-nanofluid flow for an arbitrarily inclined plate with vertical inclination γ and let the axes x and y are along the surface and perpendicular to it, respectively (see Fig. 1). The convective variation in temperature from the wall to the ambient fluid is deemed moderate ($< 40 \,^\circ$C) and an outer magnetic field normal to x-axis is applied under thermal sink/source and radiation effects. Using Oberbeck–Boussinesq approximation, the equations representing the physical characteristics of the flow become[10,51,52]

$$\overrightarrow{\nabla}.\overrightarrow{q} = 0; \overrightarrow{q} \equiv (u, v), \tag{9}$$

$$\overrightarrow{q}.\overrightarrow{\nabla} u = \frac{1}{\rho_{hnf}}\frac{\partial}{\partial y}\left(\mu_{hnf}\frac{\partial u}{\partial y}\right) + \frac{g(\rho\beta)_{hnf}\cos\gamma}{\rho_{hnf}}(T - T_\infty) - \frac{\sigma_{hnf}B_0^2}{\rho_{hnf}}(u - U_\infty), \tag{10}$$

Shape	Sphericity (Ω)	Shape factor (sf)
Spherical	1	3
Bricks	0.81	3.7
Cylindrical	0.62	4.9
Platelets	0.52	5.7
Blade	0.36	8.6

Table 2. Nanoparticles' shape and sphericity[47,48].

Properties	Copper	Alumina
C_p (Jkg^{-1} K^{-1})	385	765
ρ (kg m^{-3})	8933	3970
k (Wm^{-1} K^{-1})	400	40
$\beta \times 10^{-5}$ K^{-1}	1.67	0.85

Table 3. Nanoparticle properties[49,50].
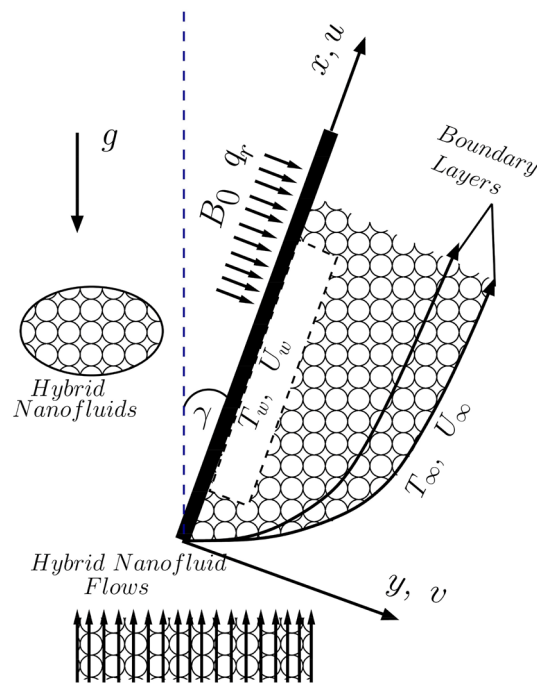
Figure 1. Flow geometry.

$$\overrightarrow{q}.\overrightarrow{\nabla} T = \frac{1}{(\rho C_p)_{hnf}} \frac{\partial}{\partial y}\left(k_{hnf}\frac{\partial T}{\partial y}\right) + \frac{Q_0}{(C_p\rho)_{hnf}}(T - T_\infty) - \frac{1}{(C_p\rho)_{hnf}}\frac{\partial q_r}{\partial y},$$

(11)

where $\rho_s = \frac{\phi_{s_1}\rho_{s_1} + \phi_{s_2}\rho_{s_2}}{\phi_{s_1} + \phi_{s_2}}$; $(C_p\rho)_s = \frac{\phi_{s_1}(C_p\rho)_{s_1} + \phi_{s_1}(C_p\rho)_{s_2}}{\phi_{s_1} + \phi_{s_2}}$" and $q_r = -\frac{4\sigma^*}{3k^*}\frac{\partial T^4}{\partial y}$. The non-linear term T^4 is approximated as $4T_\infty^3 T - 3T_\infty^4$ (Roseland approximation) and hence finally $\frac{\partial q_r}{\partial y}$ becomes $-\frac{16\sigma^* T_\infty^3}{3k^*}\frac{\partial^2 T}{\partial y^2}$.

The constraints are given by:

$$u = U_w;\ T = T_w;\ v = 0\ at\ y = 0,$$

(12)

$$u \to U_\infty;\ T \to T_\infty;\ as\ y \to \infty.$$

(13)

The following conversion variables

 4

$$\xi = \frac{x}{L}; \eta = \sqrt{\left(\frac{U}{xv_\infty}\right)}y; U = U_w + U_\infty; \epsilon = \frac{U_\infty}{U_w + U_\infty},$$

$$\psi = \sqrt{xv_\infty U}f(\xi,\eta); \frac{\partial \psi}{\partial x} = -v; \frac{\partial \psi}{\partial y} = u; f_\eta = F; u = UF,$$

$$G = \frac{T - T_\infty}{\Delta T}, \Delta T = T_w - T_\infty;$$

$$v = -\frac{1}{2}\sqrt{\frac{Uv_\infty}{x}}\left[2\xi f_\xi - \eta F + f\right]$$

are utilized to convert the Eqs. (10)–(11) into non-dimensional form:

$$\frac{\partial}{\partial \eta}\{NF_\eta\} - \xi K_1 St(F - \epsilon) + S_1\left(\frac{1}{2}fF_\eta - \xi\left(FF_\xi - f_\xi F_\eta\right)\right) + \lambda \xi S_2 G = 0, \tag{14}$$

$$\frac{\partial}{\partial \eta}\left\{\frac{N}{(Pr)_f}P_5 G_\eta\right\} + \frac{N}{(Pr)_f}R_1 G_{\eta\eta} + \xi Re QG + S_3\left(\frac{1}{2}fG_\eta + \xi\left(f_\xi G_\eta - FG_\xi\right)\right) = 0, \tag{15}$$

with

$$\begin{bmatrix} F \\ G \end{bmatrix}_{\eta=0} = \begin{bmatrix} 1 - \epsilon \\ 1 \end{bmatrix}; \begin{bmatrix} F \\ G \end{bmatrix}_{\eta=\eta_\infty} = \begin{bmatrix} \epsilon \\ 0 \end{bmatrix}. \tag{16}$$

The non-dimensional parameters buoyancy (λ), Reynolds number(Re), Grashof number(Gr), Stuart number(St), radiation(R_1), heat source(Q) are defined, respectively, as follows:

$$\lambda = \frac{Gr}{Re^2}; Re = \frac{UL}{v_\infty}; Gr = \frac{g\beta_f \Delta T L^3}{v_\infty^2}; St = \frac{\sigma_f B_0^2 L}{\rho_f U}; R_1 = \frac{16\sigma^* T_\infty^3}{3k^* k_f}; Q = \frac{Q_0 v_\infty}{(C_p\rho)_f U^2}.$$

All the other constants and coefficients are prescribed below:

$$a_1 = \frac{b_2 \Delta T}{b_1 + b_2 T_\infty}; a_2 = b_1 + b_2 T_\infty; a_3 = a_1 a_2; d_1 = c_1 + c_2 T_\infty; d_2 = c_2 \Delta T,$$

$$N = \frac{1}{1 + a_1 G}; (Pr)_f = \frac{1}{d_1 + d_2 G}; P_5 = \frac{P_1 + P_2 G}{P_3 + P_4 G}; P_6 = \frac{d_2 - a_1 d_1}{(1 + a_1 G)^2};$$

$$P_1 = a_2 \Psi_s + 2C_p d_1 - 2\phi\left(C_p d_1 - a_2 k_s\right); P_2 = a_3 k_s + 2C_p d_2 - 2\phi\left(C_p d_2 - a_3 k_s\right),$$

$$P_3 = a_2 k_s + 2C_p d_1 + \phi\left(C_p d_1 - a_2 k_s\right); P_4 = a_3 k_s + 2C_p d_2 + \phi\left(C_p d_2 - a_3 k_s\right),$$

$$P_7 = \frac{P_2 P_3 - P_1 P_4}{(P_3 + P_4 G)^2}; P_8 = -a_1 \frac{(d_2 - a_1 d_1)}{(1 + a_1 G)^3}; P_9 = -P_4 \frac{(P_2 P_3 - P_1 P_4)}{(P_3 + P_4 G)^3},$$

$$S_1 = \left\{1 - \left(1 - \frac{(\rho)_{s_1}}{(\rho)_f}\right)\phi_{s_1} - \left(1 - \frac{(\rho)_{s_2}}{(\rho)_f}\right)\phi_{s_2}\right\}\sqrt{(1-\phi)^5},$$

$$S_2 = \left\{1 - \left(1 - \frac{(\rho\beta)_{s_1}}{(\rho\beta)_f}\right)\phi_{s_1} - \left(1 - \frac{(\rho\beta)_{s_2}}{(\rho\beta)_f}\right)\phi_{s_2}\right\}\sqrt{(1-\phi)^5},$$

$$S_3 = \left\{1 - \left(1 - \frac{(C_p\rho)_{s_1}}{(C_p\rho)_s}\right)\phi_{s_1} - \left(1 - \frac{(C_p\rho)_{s_2}}{(C_p\rho)_s}\right)\phi_{s_2}\right\},$$

$$K_1 = \left\{\frac{\sigma_f + 2\sigma_s - 2\phi\left(\sigma_f - \sigma_s\right)}{\sigma_f + 2\sigma_s + \phi\left(\sigma_f - \sigma_s\right)}\right\}\sqrt{(1-\phi)^5} \text{ where } \sigma_s = \sigma_{s_1} + \sigma_{s_2}.$$

Salient gradients. *Friction (C_{f_x}).*

$$C_{f_x} = \frac{2\mu_{hnf}\left(\frac{\partial u}{\partial y}\right)_{y=0}}{\rho_f u_e^{*2}},$$

$$\therefore \sqrt{Re}C_{f_x} = \frac{2}{(1+a_1)(1-\phi)^{2.5}}\frac{F_\eta(\xi,0)}{\sqrt{\xi}}.$$

Heat transfer (Nu_x).

$$Nu_x = \frac{xq_w}{k_f\Delta T}\left[where q_w = -k_{hnf}\left(\frac{\partial T}{\partial y}\right)_{y=0}\right],$$

$$\Rightarrow Nu_x = \frac{xk_{hnf}\left(\frac{\partial T}{\partial y}\right)_{y=0}}{k_f\Delta T},$$

$$\therefore \frac{Nu_x}{\sqrt{Re}} = -\sqrt{\xi}P_5 G_\eta(\xi,0).$$

Generation of entropy

The EG model for MHD hybrid nanofluid can be written as[53]:

$$S_{gen} = \underbrace{\left(\frac{1}{T_\infty^2}\left(k_{hnf}\left(\frac{\partial T}{\partial y}\right)^2 + \frac{16\sigma^* T_\infty^3}{3k^*}\left(\frac{\partial T}{\partial y}\right)^2\right)\right)}_{HTI} + \underbrace{\left(\frac{\mu_{hnf}}{T_\infty}\left(\frac{\partial u}{\partial y}\right)^2 + \frac{\sigma_{hnf}B_0^2}{T_\infty}u\right)}_{FFI}.$$

The first brace (HTI) includes the terms representing irreversibility for heat transfer, terms inside second brace (FFI) conveys the irreversibility for fluid friction. The characteristics entropy rate $S_0 = \frac{\Delta T^2 k_f}{L^2 T_\infty^2}$ is utilized to get the dimensionless form (S_G) of total entropy (S_{gen}) i.e., $S_G = \frac{S_{gen}}{S_0} = N_1 + N_2$ where

$$N_1 = \frac{HTI}{S_0} = \frac{1}{\xi}[P_5 + R]ReG_\eta^2,$$

$$N_2 = \frac{FFI}{S_0} = \left(\frac{1}{\sqrt{(1-\phi)^5}}\frac{F_\eta^2}{\xi} + K_1 StF^2\right)\frac{ReBr}{\Omega}.$$

Here the notations $\Omega = \frac{\Delta T}{T_\infty}$, and $Br = \frac{U^2\mu_f}{k_f\Delta T}$ stand for temperature ratio and Brinkman number, respectively. The comparative study of relative irreversibility sources can be accomplished with Bejan number (Be). Mathematically, it is defined by

$$Be = \frac{HTI}{HTI + FFI} = \frac{N_1}{N_1 + N_2} = \frac{\text{Irreversiblity due to heat transfer}}{\text{total local entropy}}.$$

Numerical method and validation

The set of coupled non-linear Eqs. (14–15) has been made linear by employing the quasilinearization technique and the equations turned into

$$E_{11}^{(k)}F_{\eta\eta}^{(k+1)} + E_{12}^{(k)}F_\eta^{(k+1)} + E_{13}^{(k)}F_\xi^{(k+1)} + E_{14}^{(k)}F^{(k+1)} + E_{15}^{(k)}G_\eta^{(k+1)} + E_{16}^{(k)}G^{(k+1)} = E_{17}^{(k)}, \qquad (17)$$

$$E_{21}^{(k)}G_{\eta\eta}^{(k+1)} + E_{22}^{(k)}G_\eta^{(k+1)} + E_{23}^{(k)}G_\xi^{(k+1)} + E_{24}^{(k)}G^{(k+1)} + E_{25}^{(k)}F^{(k+1)} = E_{26}^{(k)}, \qquad (18)$$

with the boundary constraints

$$\begin{bmatrix} F^{(k+1)} \\ G^{(k+1)} \end{bmatrix}_{\eta=0} = \begin{bmatrix} 1-\epsilon \\ 1 \end{bmatrix}; \begin{bmatrix} F^{(k+1)} \\ G^{(k+1)} \end{bmatrix}_{\eta=\eta_\infty} = \begin{bmatrix} \epsilon \\ 0 \end{bmatrix}. \qquad (19)$$

Here the system (17–18) is linear for iterative indices ($k+1$) as superscripts with the coefficients:

$$E_{11} = N; E_{12} = -a_1 G_\eta N^2 + S_1 \left[f + \xi f_\xi \right]; E_{13} = -S_1 \xi F,$$

$$E_{14} = -\xi S_1 F_\xi - \xi K_1 St; E_{15} = -a_1 F_\eta N^2;$$

$$E_{16} = -a_1 F_{\eta\eta} N^2 + 2a_1^2 F_\eta G_\eta N^3 + \xi \lambda S_2;$$

$$E_{17} = -a_1 F_{\eta\eta} G N^2 - a_1 F_\eta G_\eta N^2 + 2a_1^2 F_\eta G_\eta G N^3 - S_1 \xi F F_\xi - \epsilon \xi K_1 St; E_{21} = \frac{N}{(Pr)_f} [P_5 + R_1],$$

$$E_{22} = 2G_\eta \left[P_5 P_6 + \frac{N}{(Pr)_f} P_7 \right] + S_3 \left(\frac{1}{2} f + \xi f_\xi \right); E_{23} = -S_2 \xi F,$$

$$E_{24} = G_{\eta\eta} \left[P_6 (P_5 + R_1) + \frac{N}{(Pr)_f} P_7 \right] + G_\eta^2 \left[2P_6 P_7 + P_5 P_8 + \frac{N}{(Pr)_f} P_9 \right] + \xi Q;$$

$$E_{25} = -S_2 \xi G_\xi;$$

$$E_{26} = G G_{\eta\eta} \left[(P_5 + R_1) P_6 + \frac{N}{(Pr)_f} P_7 \right] + G_\eta^2 \left[P_5 P_6 + \frac{N}{(Pr)_f} P_7 \right] - S_2 \xi F G_\xi + G G_\eta^2 \left[2P_6 P_7 + P_5 P_8 + \frac{N}{(Pr)_f} P_9 \right];$$

At this point, the following finite difference (implicit) schemes

$$F_{\eta\eta} = \frac{\left(F_{m,n-1} - 2F_{m,n} + F_{m,n+1} \right)}{(h)^2},$$

$$F_\eta = \frac{\left(F_{m,n+1} - F_{m,n-1} \right)}{2h},$$

$$F_\xi = \frac{\left(F_{m,n} - F_{m-1,n} \right)}{k},$$

transform Eqs. (17–18) into a set of algebraic equations as:

$$A_n W_{m,n-1} + B_n W_{m,n} + C_n W_{m,n+1} = D_n; \left(2 \leq n \leq \overline{N} \right), \tag{20}$$

for fixed m, where $\overline{N}$ is the number intervals of this mesh system and the vectors, coefficient matrices are:

$$W_{m,n} = \begin{bmatrix} F \\ G \end{bmatrix}_{m,n}; D_n = \begin{bmatrix} d_1 \\ d_2 \end{bmatrix}_n; A_n = \begin{bmatrix} a_{11} & a_{12} \\ a_{21} & a_{22} \end{bmatrix}_n;$$

$$B_n = \begin{bmatrix} b_{11} & b_{12} \\ b_{21} & b_{22} \end{bmatrix}_n; C_n = \begin{bmatrix} c_{11} & c_{12} \\ c_{21} & c_{22} \end{bmatrix}_n,$$

where the entries of A_n, B_n, C_n, and D_n are defined as:

$$a_{11} = E_{11} - \frac{h}{2} E_{12}, a_{12} = -\frac{h}{2} E_{12},$$

$$a_{21} = 0, a_{22} = E_{21} - \frac{h}{2} E_{22},$$

$$b_{11} = -2E_{11} + \frac{h^2}{k} E_{13} + h^2 E_{14}, b_{12} = h^2 E_{16},$$

$$b_{21} = h^2 E_{25}, b_{22} = -2E_{21} + \frac{h^2}{k} E_{23} + h^2 E_{24},$$

$$c_{11} = E_{11} + \frac{h}{2} E_{12}, c_{12} = \frac{h}{2} E_{15},$$

Pr	2	5	7	10	100
Soundalgekar and Murty[54]	0.6831	–	–	1.6808	–
Chen[55]	0.68324	–	1.38619	1.68008	5.54450
Singh et al.[56]	0.6830	1.151	1.386	1.6801	5.5450
Present results	0.6831	1.1512	1.3861	1.6801	5.5448

Table 4. Comparison of current results with available works[54–56] in literature for the case of steady-state with $\epsilon = 0, \phi = 0, \gamma = 0, \lambda = 0, B_0 = 0, q_r = 0, Q_0 = 0$ for $-G_\eta(0)$ at $\eta = 0$.

$$c_{21} = 0, c_{22} = E_{21} + \frac{h}{2}E_{22},$$

$$d_1 = h^2 E_{17} + \frac{h^2}{k}E_{13}F_{m-1,n}, d_2 = h^2 E_{26} + \frac{h^2}{k}E_{23}G_{m-1,n},$$

W_1 and $W_{\overline{N}+1}$ at the boundaries (at $\eta = 0$ and $\eta = \eta_\infty$) become:

$$W_1 = \begin{bmatrix} F \\ G \end{bmatrix}_{m,\eta=0} = \begin{bmatrix} 1-\epsilon \\ 1 \end{bmatrix}; W_{\overline{N}+1} = \begin{bmatrix} F \\ G \end{bmatrix}_{m,\eta=\eta_\infty} = \begin{bmatrix} \epsilon \\ 0 \end{bmatrix}. \quad (21)$$

Hereafter, Varga's algorithm[34], as defined below, is used to solve Eqs. (20) with constraints given by Eq. (21).

$$W_n = -E_n W_{n+1} + J_n, 1 \le n \le \overline{N},$$

where $E_n = \{B_n - A_n E_{n-1}\}^{-1} C_n$;

$$J_n = \{B_n - A_n E_{n-1}\}^{-1}\{D_n - A_n J_{n-1}\}; 2 \le n \le \overline{N},$$

$$E_1 = E_{\overline{N}+1} = \begin{bmatrix} 0 & 0 \\ 0 & 0 \end{bmatrix}, J_1 = \begin{bmatrix} 1-\epsilon \\ 1 \end{bmatrix}, J_{\overline{N}+1} = \begin{bmatrix} \epsilon \\ 0 \end{bmatrix}.$$

The numerical solutions are reached under the strict convergence criterion

$$\left(Max\left\{\left|(F_\eta)_w^{k+1} - (F_\eta)_w^k\right|, \left|(G_\eta)_w^{k+1} - (G_\eta)_w^k\right|\right\} < 10^{-4}\right),$$

and compared in Table 4 with previously published works[54–56] and found in a friendly match-up (see Table 4).

Results and discussion

The investigation of bi-convective MHD flow in light of temperature-sensorial water properties with radiation, thermal suction/injection effects is accomplished in this manuscript considering $Cu + Al_2O_3$/water hybrid nanofluid as working fluid. The acquired outcomes are featured out graphically to analyse the flow features, transport characteristics and energy distribution in comprehensive approach.

Velocity. Figure 2 is plotted to display the variable behaviour of the flow intensity ($F(\xi, \eta)$) against the buoyancy force λ. It may be noted that $F(\xi, \eta)$ increases with λ, sometimes overshoot occurs. In the physical aspect, assisting buoyancy force always surpluses pressure gradient in flow and enhances flow intensity. As numerical supporting evidence, it is seen for $\lambda = 1$ and $\lambda = 2$ at $\xi = 0.5, \eta = 1.40$ that the velocity overshoots are 15% and 33%, respectively. In contrast, $F(\xi, \eta)$ decreases for $\lambda < 0$, and in this case, for $\lambda = -1.0$ backflow is recorded within the region $0.0 < \eta \le 0.85, \xi = 0.5$.

Temperature. The changes in temperature-profile ($G(\xi, \eta)$) against the variations of thermal sink/source (Q) is elaborated graphically in Fig. 3. Since the heat source ($Q > 0$) is kept in the BL to enhance heat energy, $G(\xi, \eta)$-enhancement concerning $Q > 0$ is unambiguous. Specifically, at $\xi = 0.45, \eta = 0.5$, varying Q from 0.0 to 0.3 and 0.0 to -0.3, $G(\xi, \eta)$-profile increases and decreases, respectively, by 8% and 39%.

Gradients. *Skin friction.* The variation characteristics of friction coefficient ($\sqrt{Re}C_{fx}$) against different magnitudes of St and ϕ are demonstrated in Fig. 4, which reflects that $\sqrt{Re}C_{fx}$ is a decreasing function of St but an increasing function of ϕ. The Lorentz's force associated with St is active to detract the BL region's flow intensity, and thus friction gets dissipated. On the other hand, enhancement of tiny nanoparticles in the fluid causes richer mass density and thus increases hybrid nanofluid's friction forces and finally, $\sqrt{Re}C_{fx}$ increases. At the instant $\xi = 0.5$ with $\phi = 0.025$ enhancing St of strengths 0.3 and 0.6 from 0, $\sqrt{Re}C_{fx}$ reduces by 48% and 87%, respectively.
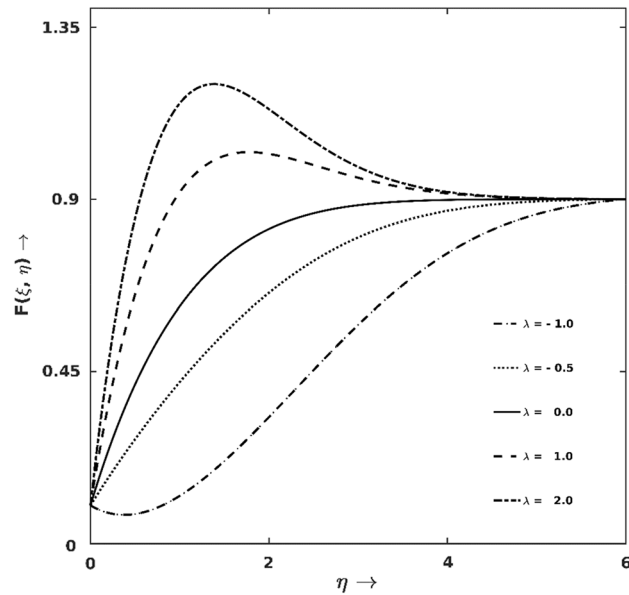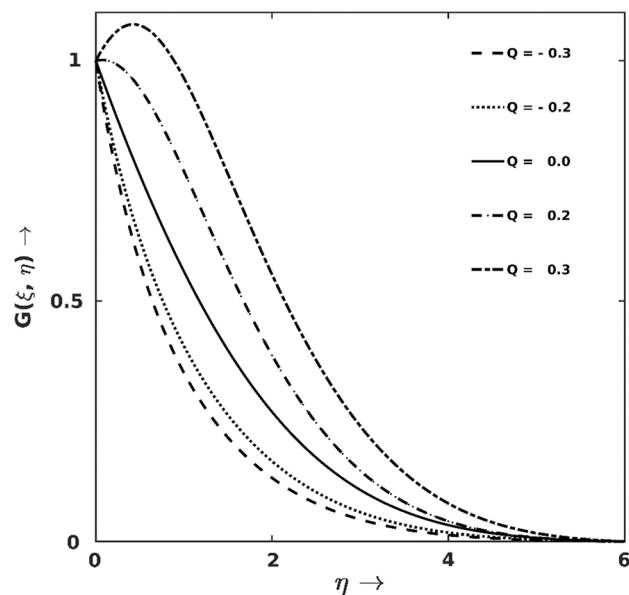
Figure 2. λ effect on F.

Figure 3. Q effect on G.

Nusselt number. The corresponding impact of St on thermal transport performance $(\frac{Nu_x}{\sqrt{Re}})$ in combination with nanoparticles' shape effects are portrayed in Fig. 5. The results indicate that the outlying force field (St) has a destructive impact on $\frac{Nu_x}{\sqrt{Re}}$, and among all the considered shapes, spherical-shaped nanoparticles affect most. In particular at $\xi = 0.5$, the decrement in sphericity Ω (i.e., increment in $sf = \frac{3}{\Omega}$) from 1.0 to 0.36 enhances $\frac{Nu_x}{\sqrt{Re}}$ almost by 7%.

Figure 6 depicts the effects of thermal radiation (R_1) on local thermal transport coefficient $(\frac{Nu_x}{\sqrt{Re}})$ and it is clearly visible in the graph that $\frac{Nu_x}{\sqrt{Re}}$ is a decreasing function of R_1. Basically, the increasing magnitude of R_1 directly enhances systems' temperature, and the fluid in BL tries to become thermally equipoise. Hence temperature gradient gets reduced, which results in less thermal transport. At the instant $\xi = 1.0$, reduction in $\frac{Nu_x}{\sqrt{Re}}$ is 35% for imposing R_1 of strength 1.0.
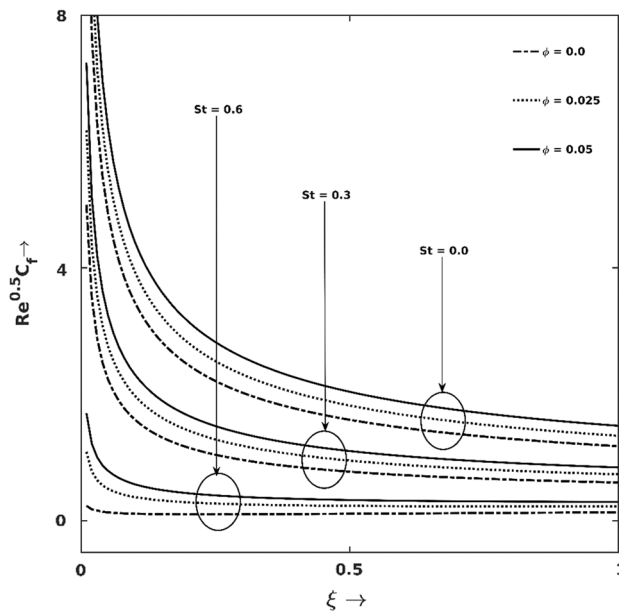
Figure 4. Friction coefficient ($\sqrt{Re}C_{fx}$) graph for different St and ϕ.
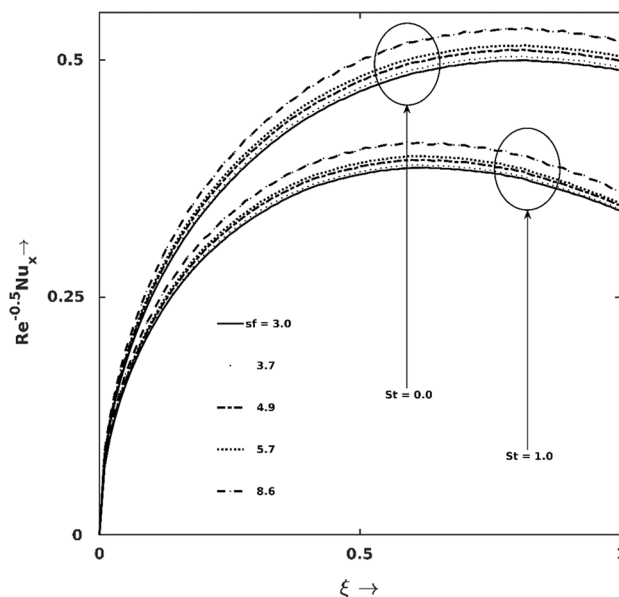
Figure 5. Nusselt number $\left(\frac{Nu_x}{\sqrt{Re}}\right)$ graph for different St and nanoparticles' shape factor (sf).

Entropy production and Bejan lines. Figures 7, 8, 9, 10, 11 and 12 illuminate the contributions of different salient parameters on the productions of irreversible heats (entropy production S_G) and their respective shares on gross entropy. Figure 7 indicates that the rate of S_G-production increases with Re, but Re's contribution on S_G is immensely high at the surface proximity. Physically, augmentation of Re increases the entropy generation S_G due to fluid friction and heat transport (via inertia). For higher Re, fluid inertia augments thermal transport, i.e., HTI takes over the other irreversibility sources. In contrast for lower Re, as viscous force is high, FFI dominates the total S_G close to the wall. Thus, the friction force gets mitigated within the boundary layer and HTI takes over the dominant place. Hence, Bejan lines for lower Re intersect the lines for higher Re within the boundary layer.

Moreover, all the Bejan lines converge to zero at the boundary layer edge since HTI gradually reduces to zero at the edge of the boundary layer. It is also noticed that the surface plays a high intense S_G-production source and is evidenced by the following specific calculation: at $\eta = 0.0$, S_G elevates by 46% for varying Re in $10 - 12.5$ while the change is only 20% at $\eta = 1.5$ for the same variation of Re.
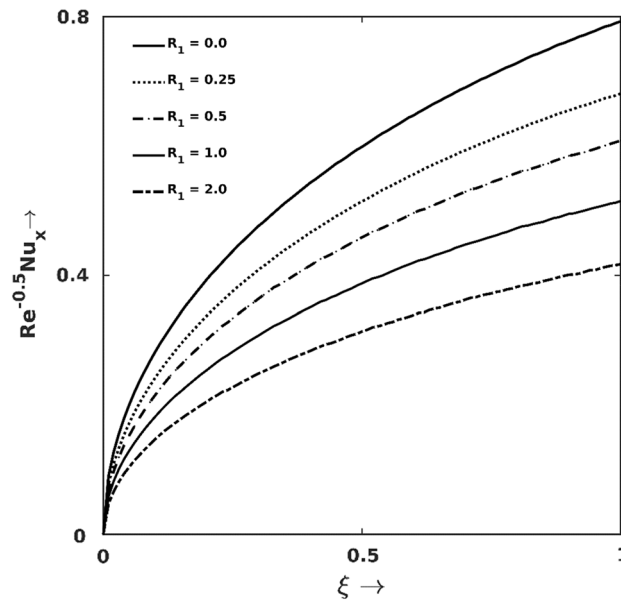
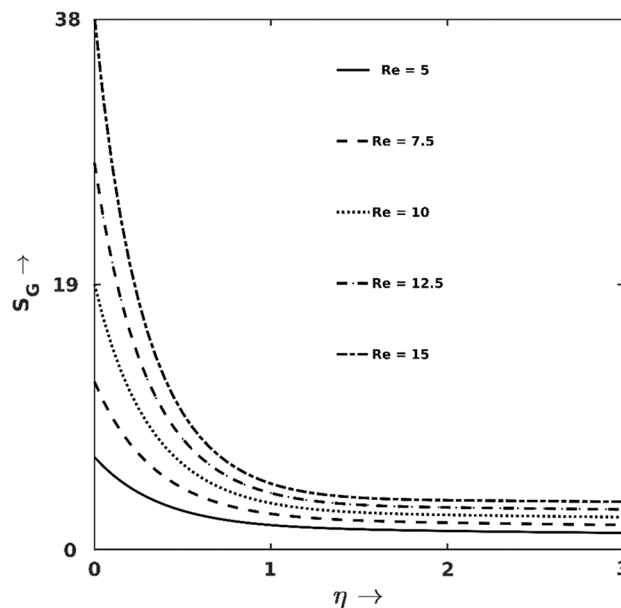**Figure 6.** Nusselt number $\left(\frac{Nu_x}{\sqrt{Re}}\right)$ graph for different R_1.

Figure 7. *Re* effect on S_G.

Figures 9 and 10 manifested the S_G-production and Bejan line regarding different magnitudes of viscous heating (Br). As exhibited in Fig. 12, higher Br boosts S_G at the wall's proximity but discloses an opposite trend away from the surface. Lifting up the Br value causes added viscous force to the fluid and enhances frictional heating. This frictional heating turns up excessive S_G-production. This fact is also evidenced in Fig. 10, which shows lifted down Bejan lines for higher Br, which physically represents that most S_G-productions are due to frictional heating (FFI), the associated entropy produced in other modes (i.e., HTI and DI) are comparatively less. Analysing the result data, 32% enhancement in S_G is noticed for changing Br from 0.01 to 0.2 at $\eta = 0.5$.

Figures 11 and 12 demonstrate how S_G and Be get affected under the forces of buoyancy (λ). As one can point out from Fig. 11 that S_G shows a growing trend for the increase of λ. The earlier discussions proclaimed that larger λ pushes the fluids to move faster generates excessive friction at the wall and hence the irreversibility enhances (via FFI, as shown in Fig. 12). Since the buoyancy effect is induced by the thermal imbalance between the wall and neighbouring fluids, the effect of λ is predominantly noticeable at the wall proximity. Hence, the irreversibilities due to λ variation vanish at the boundary layer edge and all S_G-lines converge at the edge of the boundary layer.
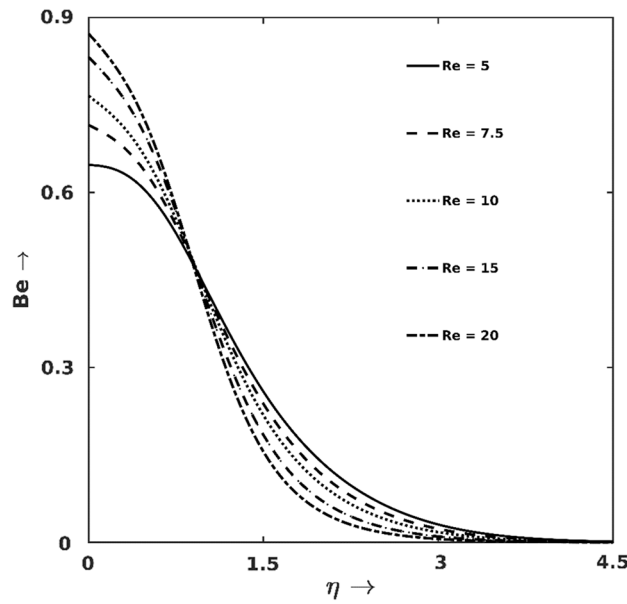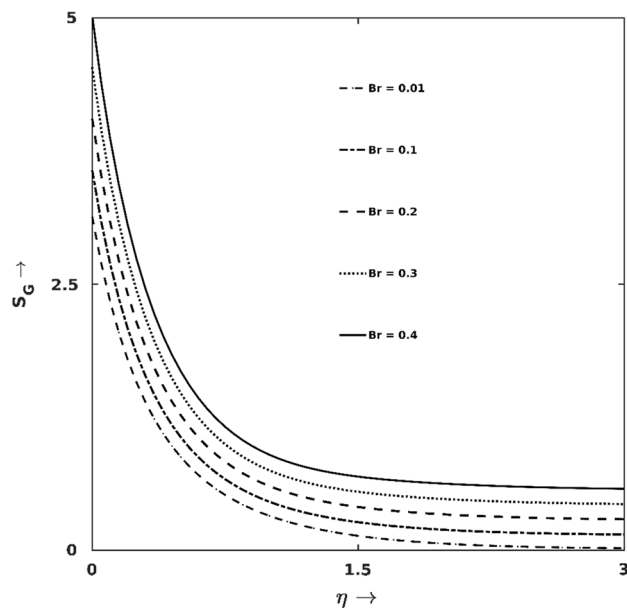
Figure 8. *Re* effect on *Be*.

Figure 9. *Br* effect on S_G.

Conclusions

This paper performs an analysis on a hybrid nano-liquid flow for an inclined surface under various realistic and practical physical situations by considering the basic temperature-sensorial inheriting characteristics (thermos-physical) of base fluid water. The bearings of flow features, thermal transport characteristics, and EG of magnet-ized bi-convective hybrid nano-liquid flow with nanoparticles' sphericity, radiation and thermal source/sink effects are studied in this investigation. The immensely nonlinear PDEs are changed into suitable form and then into linear form utilizing compatible transformation and quasilinearization techniques, respectively. Hereafter, implicit difference methods changed the resulting equations into a matrix system which was further solved by Vargas' block matrix iterative method. The acquired results of this study are manifested in graphs and discussed in details. The concluding remarks from the investigated results are summarized and expressed with numerical percentile calculations as observed in this specific study:
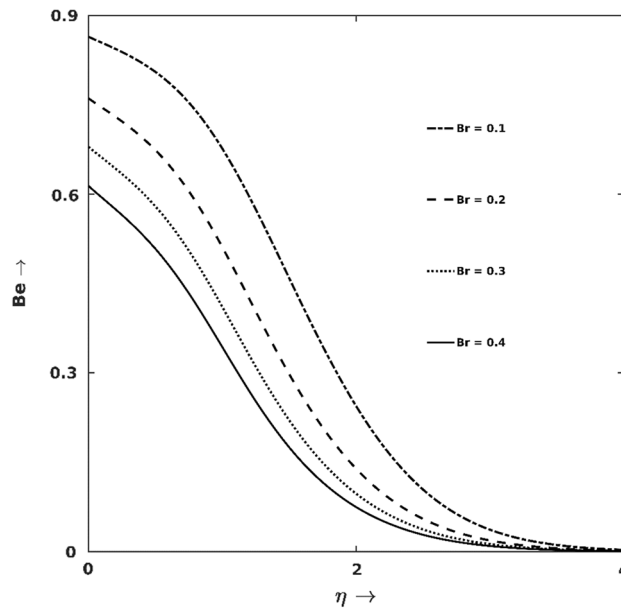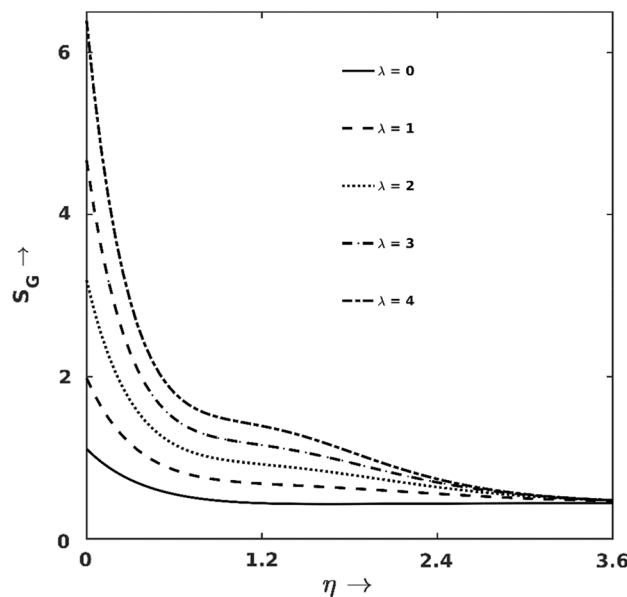
Figure 10. *Br* effect on *Be*.

Figure 11. λ effect on S_G.

i. The trend of $F(\xi, \eta)$-profiles shows increment for assisting ($\lambda > 0$) and decrement for opposing buoyancy ($\lambda < 0$). In particular, for $\lambda = 2$, almost 33% overshoot is observed when at $\eta = 1.40, \xi = 0.5$ but in contradiction almost 25% backflow is noticed at $\eta = 0.4, \xi = 0.5$ when $\lambda = -1.0$.

ii. Temperature-profile ($G(\xi, \eta)$) rising along with the heat source strength Q.

iii. Significant reduction in friction is happened under the effect of MHD parameter St. In particular, at $\xi = 1.0$, imposing St of magnitude 0.6 on $\sqrt{Re}C_{fx}$ deduces it almost by 87%.

iv. Friction $\left(\sqrt{Re}C_{fx}\right)$ escalates for increasing the amount of nanoparticles, specifically, $\sqrt{Re}C_{fx}$ enhances approximately by 40% for increasing ϕ from 0.0 to 0.05.

v. Thermal transport coefficient mitigates under the effect of MHD parameter St. Particularly, at $\xi = 1.0$, imposing St of magnitude 1.0 on $\frac{Nu_x}{\sqrt{Re}}$ deduces it almost 30%.

vi. The heat transport is enhanced by 7% as the nanoparticles' sphericity ($\Omega = \frac{3}{sf}$) goes down from $\Omega = 1$ to $\Omega = 0.36$.
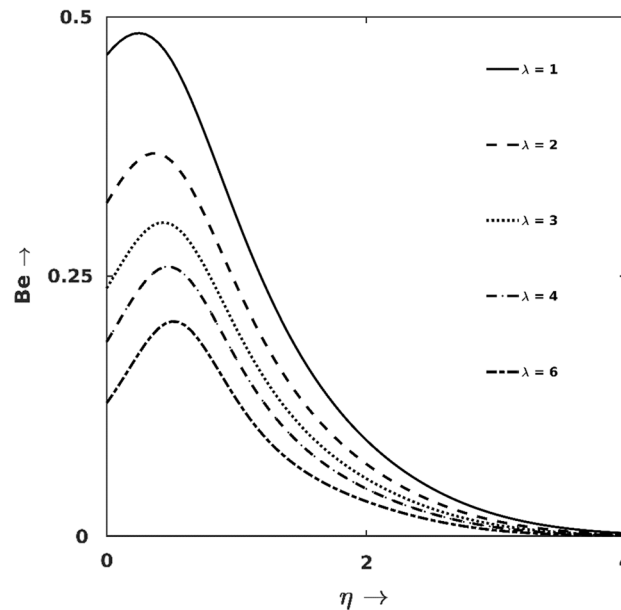
Figure 12. λ effect on S_G.

vii. The thermal transport rate $\frac{Nu_x}{\sqrt{Re}}$ is drastically affected by radiation (R_1). Numerical enumeration on $\frac{Nu_x}{\sqrt{Re}}$ at $\xi = 1.0$ exposes 35% redution for applying R_1 of strength 1.0.

viii. The rate of entropy production (S_G) is cumulative for enhancing estimations of Re, Br and λ.

ix. Irreversibility owing to frictional heating (*FFI*) takes the dominant place over the other sources (*HTI, DI*) as Br and λ increases.

x. Irreversibility due to *HTI* plays the major role in S_G-production over other sources (*FFI, DI*) for higher Re and lower magnitudes of Br and λ.

xi. The bounding surface acts as a strong source of S_G-production.

xii. The enhancing variation in S_G is 58% for changing λ in the range $1.0 - 4.0$.

Data availability

All data generated or analyzed during this study are included in this published article. Also, the datasets used and/or analyzed during the current study are available from the corresponding author on reasonable request.

References

1. Fujii, T. & Imura, H. Natural-convection heat transfer from a plate with arbitrary inclination. *Int. J. Heat Mass Transf.* **15**, 755–767 (1972).
2. Lloyd, J. R., Sparrow, E. M. & Eckert, E. R. G. Laminar, transition and turbulent natural convection adjacent to inclined and vertical surfaces. *Int. J. Heat Mass Transf.* **15**, 457–473 (1972).
3. Chen, T. S., Tien, H. C. & Armaly, B. F. Natural convection on horizontal, inclined, and vertical plates with variable surface temperature or heat flux. *Int. J. Heat Mass Transf.* **29**, 1465–1478 (1986).
4. Al-Arabi, M. & Sakr, B. Natural convection heat transfer from inclined isothermal plates. *Int. J. Heat Mass Transf.* **31**, 559–566 (1988).
5. Lewandowski, W. M. Natural convection heat transfer from plates of finite dimensions. *Int. J. Heat Mass Transf.* **34**, 875–885 (1991).
6. Jayaraj, S. Thermophoresis in laminar flow over cold inclined plates with variable properties. *Heat Mass Transf.* **30**, 167–173 (1995).
7. Ramadan, H. M. & Chamkha, A. J. Two-phase free convection flow over an infinite permeable inclined plate with non-uniform particle-phase density. *Int. J. Eng. Sci.* **37**, 1351–1367 (1999).
8. Chamkha, A. J. & Ramadan, H. M. Analytical solution for free convection of a particulate suspension past an infinite vertical surface. *Int. J. Eng. Sci.* **36**, 49–60 (1997).
9. Chamkha, A. J., Issa, C. & Khanafer, K. Natural convection from an inclined plate embedded in a variable porosity porous medium due to solar radiation. *Int. J. Therm. Sci.* **41**, 73–81 (2002).
10. Alam, M. S., Rahman, M. M. & Sattar, M. A. Effects of variable suction and thermophoresis on steady MHD combined free-forced convective heat and mass transfer flow over a semi-infinite permeable inclined plate in the presence of thermal radiation. *Int. J. Therm. Sci.* **47**, 758–765 (2008).
11. Alam, M. S., Rahman, M. M. & Sattar, M. A. On the effectiveness of viscous dissipation and Joule heating on steady Magnetohydrodynamic heat and mass transfer flow over an inclined radiate isothermal permeable surface in the presence of thermophoresis. *Commun. Nonlinear. Sci. Numer. Simul.* **14**, 2132–2143 (2009).
12. Das, K. Slip effects on heat and mass transfer in MHD micropolar fluid flow over an inclined plate with thermal radiation and chemical reaction. *Int. J. Numer. Methods Fluids.* **70**, 96–113 (2012).

13. Rana, P., Bhargava, R. & Bég, O. A. Numerical solution for mixed convection boundary layer flow of a nanofluid along an inclined plate embedded in a porous medium. *Comput. Math. Appl.* **64**, 2816–2832 (2012).

14. Das, S., Jana, R. N. & Makinde, O. D. Magnetohydrodynamic mixed convective slip flow over an inclined porous plate with viscous dissipation and Joule heating. *Alex. Eng. J.* **54**, 251–261 (2015).

15. Khademi, R., Razminia, A. & Shiryaev, V. I. Conjugate-mixed convection of nanofluid flow over an inclined flat plate in porous media. *Appl. Math. Comput.* **366**, 124761 (2020).

16. Krishna, M. V. Hall and ion slip effects on radiative MHD rotating flow of Jeffreys fluid past an infinite vertical flat porous surface with ramped wall velocity and temperature. *Int. Commun. Heat Mass Transf.* **126**, 105399 (2021).

17. Alsabery, A. I., Sheremet, M. A., Chamkha, A. J. & Hashim, I. J. S. R. MHD convective heat transfer in a discretely heated square cavity with conductive inner block using two-phase nanofluid model. *Sci. Rep.* **8**, 1–23 (2018).

18. El-Zahar, E. R., Rashad, A. M., Saad, W. & Seddek, L. F. Magneto-hybrid nanofluids flow via mixed convection past a radiative circular cylinder. *Sci. Rep.* **10**, 1–13 (2020).

19. Bilal, M. *et al.* Dissipated electroosmotic EMHD hybrid nanofluid flow through the micro-channel. *Sci. Rep.* **12**, 1–5 (2022).

20. Ramzan, M. & Alotaibi, H. Variable viscosity effects on the flow of MHD hybrid nanofluid containing dust particles over a needle with Hall current—A Xue model exploration. *Commun. Theor. Phys.* https://doi.org/10.1088/1572-9494/ac64f2 (2022).

21. Bhatti, M. M., Bég, O. A. & Abdelsalam, S. I. Computational framework of magnetized MgO–Ni/water-based stagnation nanoflow past an elastic stretching surface: Application in solar energy coatings. *J. Nanomater.* **12**, 1049 (2022).

22. Zhang, L., Bhatti, M. M., Michaelides, E. E., Marin, M. & Ellahi, R. Hybrid nanofluid flow towards an elastic surface with tantalum and nickel nanoparticles, under the influence of an induced magnetic field. *Eur. Phys. J. Spec. Top.* https://doi.org/10.1140/epjs/s11734-021-00409-1 (2021).

23. Ramesh, G. K., Chamkha, A. J. & Gireesha, B. J. MHD mixed convection flow of a viscoelastic fluid over an inclined surface with a nonuniform heat source/sink. *Can. J. Phys.* **91**, 1074–1080 (2013).

24. Bilal, S. *et al.* Significance of induced hybridized metallic and non-metallic nanoparticles in single-phase nano liquid flow between permeable disks by analyzing shape factor. *Sci. Rep.* **12**, 1–6 (2022).

25. Chu, Y. M., Bashir, S., Ramzan, M. & Malik, M. Y. Model-based comparative study of magnetohydrodynamics unsteady hybrid nanofluid flow between two infinite parallel plates with particle shape effects. *Math. Methods Appl. Sci.* https://doi.org/10.1002/mma.8234 (2022).

26. Rashad, A. M., Chamkha, A. J., Ismael, M. A. & Salah, T. Magnetohydrodynamics natural convection in a triangular cavity filled with a Cu-Al₂O₃/water hybrid nanofluid with localized heating from below and internal heat generation. *J. Heat Transf.* **140**, 072502 (2018).

27. Maskeen, M. M., Zeeshan, A., Mehmood, O. U. & Hassan, M. Heat transfer enhancement in hydromagnetic alumina–copper/water hybrid nanofluid flow over a stretching cylinder. *J. Therm. Anal. Calorim.* **138**, 1127–1136 (2019).

28. Shoaib, M. *et al.* Numerical investigation for rotating flow of MHD hybrid nanofluid with thermal radiation over a stretching sheet. *Sci. Rep.* **10**, 1–15 (2020).

29. Ashwinkumar, G. P., Samrat, S. P. & Sandeep, N. Convective heat transfer in MHD hybrid nanofluid flow over two different geometries. *Int. Commun. Heat Mass Transf.* **127**, 105563 (2021).

30. Rajesh, V., Sheremet, M. A. & Öztop, H. F. Impact of hybrid nanofluids on MHD flow and heat transfer near a vertical plate with ramped wall temperature. *Case Stud. Therm. Eng.* **28**, 101557 (2021).

31. Bhatti, M. M., Öztop, H. F., Ellahi, R., Sarris, I. E. & Doranehgard, M. H. Insight into the investigation of diamond (C) and Silica (SiO₂) nanoparticles suspended in water-based hybrid nanofluid with application in solar collector. *J. Mol. Liq.* **357**, 119–134 (2022).

32. Pattnaik, P. K., Bhatti, M. M., Mishra, S. R., Abbas, M. A. & Bég, O. A. Mixed convective-radiative dissipative magnetized micropolar nanofluid flow over a stretching surface in porous media with double stratification and chemical reaction effects: ADM-Padé computation. *J. Math.* https://doi.org/10.1155/2022/9888379 (2022).

33. Ramzan, M., Riasat, S. & Alotaibi, H. EMHD hybrid squeezing nanofluid flow with variable features and irreversibility analysis. *Phys. Scr.* **97**, 025705 (2022).

34. Reddy, P. B. A. Biomedical aspects of entropy generation on electromagnetohydrodynamic blood flow of hybrid nanofluid with nonlinear thermal radiation and non-uniform heat source/sink. *Eur. Phys. J. Plus.* **135**, 1–30 (2020).

35. Shaw, S., Dogonchi, A. S., Nayak, M. K. & Makinde, O. D. Impact of entropy generation and nonlinear thermal radiation on Darcy–Forchheimer flow of MnFe₂O₄-Casson/water nanofluid due to a rotating disk: Application to brain dynamics. *Arab. J. Sci. Eng.* **45**, 5471–5490 (2020).

36. Ahmad, S., Nadeem, S. & Ullah, N. Entropy generation and temperature-dependent viscosity in the study of SWCNT–MWCNT hybrid nanofluid. *Appl. Nanosci.* **10**, 5107–5119 (2020).

37. Khan, M. W. A., Khan, M. I., Hayat, T. & Alsaedi, A. Entropy generation minimization (EGM) of nanofluid flow by a thin moving needle with nonlinear thermal radiation. *Phys. B Condens. Matter.* **534**, 113–119 (2018).

38. Khan, N. S. *et al.* Entropy generation in bioconvection nanofluid flow between two stretchable rotating disks. *Sci. Rep.* **10**, 1–26 (2020).

39. Kolsi, L., Hussein, A. K., Borjini, M. N., Mohammed, H. A. & Aïssia, H. B. Computational analysis of three-dimensional unsteady natural convection and entropy generation in a cubical enclosure filled with water-Al₂O₃ nanofluid. *Arab. J. Sci. Eng.* **39**, 7483–7493 (2014).

40. Ishak, M. S., Alsabery, A. I., Hashim, I. & Chamkha, A. J. Entropy production and mixed convection within trapezoidal cavity having nanofluids and localised solid cylinder. *Sci. Rep.* **11**, 1–22 (2021).

41. Rajakumar, J., Saikrishnan, P. & Chamkha, A. Non-uniform mass transfer in MHD mixed convection flow of water over a sphere with variable viscosity and Prandtl number. *Int. J. Numer. Method Heat.* **26**, 2235–2251 (2016).

42. Lide, D. R. *CRC Handbook of Chemistry and Physics*, vol. 85. (CRC Press, 2004) ISBN-10: 0849304857, ISBN-13: 978-084930485-9

43. Varga, R. S. *Matrix Iterative Analysis* Vol. 27 (Springer, 2000).

44. Saikrishnan, P. & Roy, S. Non-uniform slot injection (suction) into water boundary layers over (i) a cylinder and (ii) a sphere. *Int. J. Eng. Sci.* **41**, 1351–1365 (2003).

45. Revathi, G., Saikrishnan, P. & Chamkha, A. Non-similar solutions for unsteady flow over a yawed cylinder with non-uniform mass transfer through a slot. *Ain Shams Eng. J.* **5**, 1199–1206 (2014).

46. Chamkha, A. J., Miroshnichenko, I. V. & Sheremet, M. A. Numerical analysis of unsteady conjugate natural convection of hybrid water-based nanofluid in a semicircular cavity. *J. Therm. Sci. Eng. Appl.* **9**, 041004 (2017).

47. Dogonchi, A. S., Selimefendigil, F. & Ganji, D. D. Magneto-hydrodynamic natural convection of CuO-water nanofluid in complex shaped enclosure considering various nanoparticle shapes. *Int. J. Numer. Method. Heat.* **29**, 1663–1679 (2019).

48. Timofeeva, E. V., Routbort, J. L. & Singh, D. Particle shape effects on thermophysical properties of alumina nanofluids. *J. Appl. Phys.* **106**, 014304 (2009).

49. Alsabery, A. I., Sidik, N. A. C., Hashim, I. & Muhammad, N. M. Impacts of two-phase nanofluid approach toward forced convection heat transfer within a 3D wavy horizontal channel. *Chin. J. Phys.* https://doi.org/10.1016/j.cjph.2021.10.049 (2022).

50. Abu-Nada, E., Masoud, Z. & Hijazi, A. Natural convection heat transfer enhancement in horizontal concentric annuli using nanofluids. *Int. Commun. Heat Mass Transf.* **35**, 657–665 (2008).

51. Kuznetsov, A. V. & Nield, D. A. Natural convective boundary-layer flow of a nanofluid past a vertical plate. *Int. J. Therm. Sci.* **49**, 243–247 (2010).

52. Reddy, P. S. & Chamkha, A. Heat and mass transfer analysis in natural convection flow of nanofluid over a vertical cone with chemical reaction. *Int. J. Numer. Method Heat.* **27**, 2–22 (2017).
53. Abbas, S. Z. *et al.* Fully developed entropy optimized second order velocity slip MHD nanofluid flow with activation energy. *Comput. Methods. Programs. Biomed.* **190**, 105362 (2020).
54. Soundalgekar, V. M. & Ramana Murty, T. V. Heat transfer in flow past a continuous moving plate with variable temperature. *WaÈrme-und stoffuÈbertragung.* **14**, 91–93 (1980).
55. Chen, C. H. Laminar mixed convection adjacent to vertical, continuously stretching sheets. *Heat Mass transf.* **33**, 471–476 (1998).
56. Singh, A. K., Singh, A. K. & Roy, S. Analysis of mixed convection in water boundary layer flows over a moving vertical plate with variable viscosity and Prandtl number. *Int. J. Numer. Method. Heat.* **29**, 602–616 (2019).

Acknowledgements

Author contributions

All authors have an equal contribution.

Competing interests

The authors declare no competing interests.

Additional information

Correspondence and requests for materials should be addressed to S.R.

Reprints and permissions information is available at www.nature.com/reprints.

Publisher's note Springer Nature remains neutral with regard to jurisdictional claims in published maps and institutional affiliations.